Separation and Purification Technology 376 (2025) 133834

Contents lists available at ScienceDirect

Separation and Purification Technology

journal homepage: www.elsevier.com/locate/seppur

Transition from clamshell to barrel shaped oil droplets on a single oleophobic fiber through periodic mechanical excitation

Florian Freese [b,*], Alexander Schwarzwälder [a], Uwe Janoske [b], Achim Dittler [a]

[a] Karlsruhe Institute of Technology, Institute of Mechanical Process Engineering and Mechanics, Straße am Forum 8, Karlsruhe, 76131, Baden-Württemberg, Deutschland, Germany
[b] Bergische Universität Wuppertal, Fakultät für Maschinenbau und Sicherheitstechnik, Gaußstraße 20, Wuppertal, 42119, Nordrhein-Westfalen, Deutschland, Germany

ARTICLE INFO

Communicated by Volodymyr Tarabara

Keywords:
Droplet
Single fiber
Vibration
CFD
Overset mesh
High-speed images

ABSTRACT

This study examines the interaction between single oil droplets and an oleophobic fiber subjected to sinusoidal mechanical excitation, with particular emphasis on the vibrational effects on the resulting droplet motion patterns. The research combines experiments providing high-speed images and CFD simulations, employing a dynamic overset grid technique, to explore various droplet motion patterns, such as pumping, swinging, vertical oscillation, rotation, and collapsing. A key finding is that fiber oscillation induces a lasting transformation, whereby clamshell-shaped droplets—typically seen on oleophobic fibers—permanently adopt a barrel shape, characteristic of oleophilic fibers, even after the excitation ceases. Despite differences in wettability, oil droplets exhibit similar motion patterns on both fiber types after their transition and prior to detachment. The results highlight the importance of droplet dynamics for optimizing coalescence and drainage in industrial settings.

1. Introduction

The interaction between liquid droplets and solid surfaces is a fundamental phenomenon in fluid mechanics and materials science, with implications across a wide range of applications, including coatings, filtration, and biomedical engineering. Due to its relevance in oil mist filtration, the wetting behavior of droplets on fibers has garnered significant attention [1].

Extensive research has been dedicated to studying droplet–fiber interactions, focusing on aspects such as contact angle and wetting behavior [2–5], droplet transport along fibers [6], droplet impact [7], coalescence, growth, and detachment [8,9], while taking into account various influencing parameters, such as surface roughness [10], advancing and receding contact angles [11,12], fiber orientation [9], external fields [13], and fluid properties. The majority of these studies use fixed in-place fibers to analyze droplet–fiber interactions. However, in various applications, such as coalescing filters, the filter, and consequently the individual fiber, may oscillate due to external forces or flow-induced vibrations.

The presence of vibrations introduces further complexity to the droplet–fiber interaction, impacting key phenomena such as adhesion, spreading, and possible detachment [14].

In this study, the droplet–fiber interaction of an already separated oil droplet on a fiber is investigated under sinusoidal mechanical excitation. The primary objective is to identify characteristic droplet motion regimes as functions of the excitation amplitude, excitation frequency, and droplet volume. These results are compared to previously reported findings for an oleophilic fiber. Characteristic motion patterns are identified through both experimental and numerical analyses. For the simulations, experimentally determined equilibrium, advancing, and receding contact angles (CAs) were implemented as boundary conditions in the overset mesh simulations, incorporating the feedback deceleration technique originally developed by [15] and later refined by [16].

It was shown for the first time that mechanical excitation can induce a transition from a clamshell-shaped droplet, typically observed on oleophobic fibers, to a barrel-shaped droplet, which is characteristic of oleophilic fibers. Consequently, the results and identified mechanisms are compared to those observed for an oleophilic fiber.

These findings shed light on filter behavior that has remained unexplained under vibrational conditions.

2. Materials and methods

2.1. Experimental setup

Fig. 1 shows the horizontally positioned fiber on an electrodynamic shaker, which subjects it to vertical sinusoidal excitation. The camera

* Corresponding author.
E-mail address: freese@uni-wuppertal.de (F. Freese).

https://doi.org/10.1016/j.seppur.2025.133834
Received 24 April 2025; Received in revised form 31 May 2025; Accepted 31 May 2025
Available online 14 June 2025

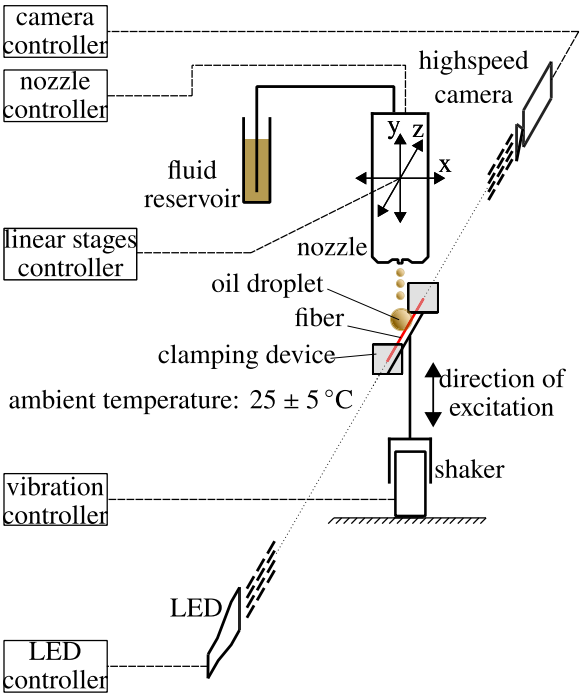

Fig. 1. Schematic diagram of the fiber vibration experiment setup.

and lighting are arranged along the fiber axis. The fiber is fixed at both ends in epoxy resin, allowing for optical access along the fiber axis. A defined liquid volume is dispensed onto the initially resting fiber using a piezoelectric nozzle, which can be precisely positioned above the fiber using an xyz-axis linear stage. Using a high-speed camera and back lighting, the droplet contour, including the fiber, is captured with high temporal resolution. The experiments were conducted at ambient pressure and a temperature of $25 \pm 5\,°C$.

2.2. Clamping device

The clamping device allows the fiber to be securely clamped on both sides within transparent resin blocks (see Fig. 2). Epoxy resin is applied on each side, sandwiched between two transparent PMMA plates positioned within a 3D printed PLA structure. The fiber is clamped with a tensile force of 2.45 N, resulting in an analytically approximated natural frequency of 3.11 kHz, which is well above the used frequencies in the investigations. A detailed derivation of this approximation can be found in Appendix.

2.3. Fiber & coating

The fiber used has a diameter of 80 µm. The core of the fiber is a stainless steel fiber manufactured by Carl Haas. An oleophobic coating, known as ProSurf and provided by Surfactis Technologies, was applied using a drop-wise method. Electrowetting — a state-of-the-art technique for precise contact angle modulation [11] — was ruled out in favor of a dropwise coating application, since the surrounding medium (air in a flow channel) is unsuitable for electrowetting. Instead, a drop-wise procedure was chosen because the fiber, once mounted in the clamping device, needed to be coated under tensile load to avoid stress-induced cracks. The coating consists of bisphosphonic compounds dissolved in a fluorinated solvent. SEM images of both the raw and coated fiber are shown in Fig. 3. For the blank fiber, a very homogeneous surface was observed, with occasional contaminants and longitudinal grooves in the sub-micrometer range. These grooves are attributed to the drawing manufacturing process. When closely examined, the coated fiber reveals visible contaminants, which are covered by the coating, resulting in an overall smoother surface compared to the raw fiber. There was no measurable change in thickness due to the application of the coating. The same coated fiber was used throughout all experiments and cleaned with isopropanol after each experiment to remove oil residues.

Table 1
Summary of all the parameters investigated.

Parameter	Value
amplitude A/mm	0.05, 0.25, 0.5, 0.75
frequency f/Hz	40, 100, 540 (@0.05 mm), 240 (@0.25 mm), 170 (@0.5 mm), 140 (@0.75 mm)
droplet volume V/nL	22, 44, 88, 177

2.4. Experimental procedure

First, a droplet is placed on top of the fiber using the piezoelectric nozzle. Subsequently, the shaker is activated, beginning a ramp-up phase in which the frequency of oscillation remains constant. During this 4-second-long ramp-up phase, the amplitude gradually increases until the desired operating point is reached. This increase in amplitude may ultimately lead to the detachment of the droplet from the fiber. Once the detachment of the droplet is observed in the live image, the camera trigger is activated, storing approximately 4 s of preceding footage (the exact duration depends on image quality and settings). If the droplet does not detach after at least 10 s excitation at the conditions of the operating point, the trigger is activated regardless. Due to this experimental procedure, direct correlation between the saved image series and the total excitation duration is not possible. Consequently, for each recorded image series, only the period duration is provided, with the start of the image series designated as time zero (see Fig. 4). As illustrated in Fig. 4, the simulations omit this ramp-up phase as this would result in computationally prohibitive simulation times.

The operating parameters used in the parameter study can be found in Table 1. A total of four amplitudes were investigated. For each amplitude, the shaker was operated at 40 Hz, 100 Hz, and a third frequency. The third frequency was selected to utilize the shaker's maximum output power, which depends on the amplitude and is 540 Hz (@0.05 mm), 240 Hz (@0.25 mm), 170 Hz (@0.5 mm) and 140 Hz (@0.75 mm).

2.5. Post-processing of the image series to determine the motion patterns of the droplet on the excited fiber

The high-speed recordings of all experiments in the parameter study were analyzed, similar to [17], by a MATLAB script identifying the droplet itself, as well as the centroids of both the droplet and the fiber. Additionally, the droplet detachment is detected. The fiber position is reconstructed based on four manually selected support points using user input for the fiber position and a sine signal with a frequency corresponding to the excitation. In the case of a recorded image series during the ramp-up phase, the increase of the amplitude is approximated linearly. This assumption is appropriate due to the few periods of excitation considered in the post-processing.

2.6. Determination of the advancing, receding, and equilibrium contact angles for the simulations

In preliminary investigations, the static and the dynamic contact angles were determined to provide boundary conditions for the simulation. The advancing and receding contact angles were determined for a droplet with a volume of 44 nL under the maximum excitation achievable by the shaker, with an amplitude of 0.05 mm and a frequency of

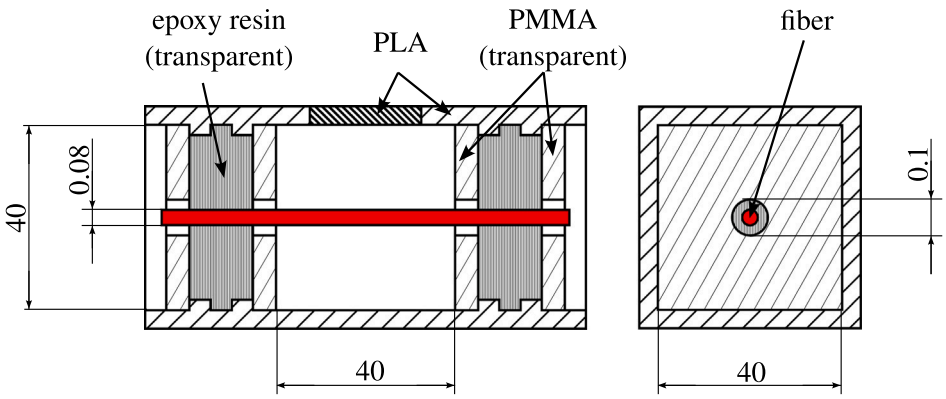

(a) Radial view of clamping device (b) Axial view of clamping device

Fig. 2. Schematic sketch of clamping device. All units are in millimeter.

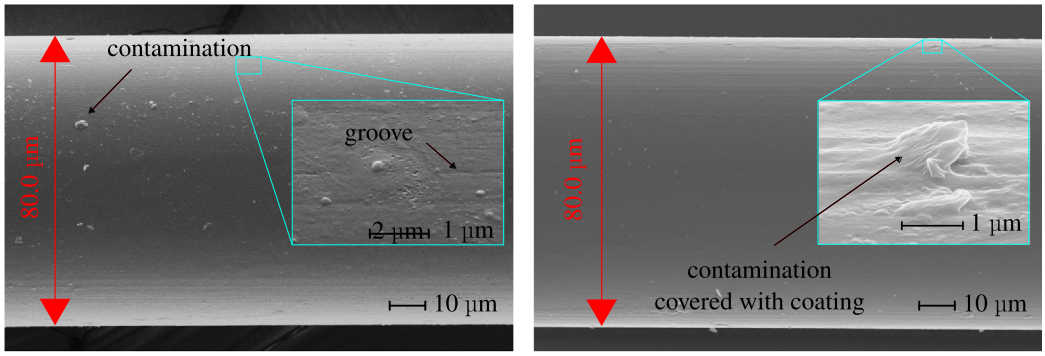

(a) Blank fiber (b) Coated fiber

Fig. 3. Comparison of the coated and uncoated fiber.

540 Hz. These excitation parameters result in a maximum acceleration of 580 $\mathrm{m\,s^{-2}}$ and were chosen to enforce maximum deformation of the droplet within the field of view. Smaller droplets were not selected, as this would result in reduced spatial resolution, and a macro lens with higher magnification does not provide a sufficient field of view. Conversely, larger droplets were swinging around the fiber after the shaker ramped up to the desired operating point. Consequently, the contact angles from an axial direction were measured exclusively for droplets with a volume of 44 nL.

A separate MATLAB script was employed to determine the contact angle of the preliminary investigations. The fiber position was manually specified for each frame. The droplet contour was detected via binarization. The droplet surface in proximity to the triple points on the fiber was then approximated by two fourth-degree polynomials utilizing 10 % of the whole droplet contour length on either side as sampling points. Afterward, the CAs were calculated using the tangent of the fitted polynomials at the triple point and the fiber on the left and right sides. The average contact angle from 8 measurements, including the values of the left and right contact angles, resulted in an advancing angle of $111 \pm 7°$, a receding angle of $76 \pm 12°$, and a static contact angle on the stationary fiber of $90 \pm 9°$ (see Fig. 5).

2.7. Numerical method

For the overset mesh simulation of the oscillating fiber with the droplet, the *overInterDyMFoam* solver included in the openFOAM® open-source software package was expanded by the implementation of the adapted feedback deceleration technique [16] (AFDT). The AFDT is a method used to model the contact angle hysteresis and to slow down the movement of the contact line by using a specified contact angle increment. This increment

$$\delta\Theta = \frac{\Theta_A - \Theta_R}{\left|cos\left(\Theta_A\right) - cos\left(\Theta_R\right)\right|} \frac{\Delta x}{\Delta y} \frac{\mu}{\sigma} \left|u_{CL}\right| \tag{1}$$

depends on parameters of the droplet–fiber system (Θ_A, Θ_R, μ_s, σ), the computational grid (Δx, Δy) and the contact line velocity (u_{CL}). The overset method enables the connection of two or more overlapping computational grids by interpolation. Leveraging this method facilitates the use of body-fitted grids for independent objects submerged in one or multiple fluids. The movement of the fiber is integrated through an overset mesh, which moves dynamically within a coarser background mesh. Furthermore, the droplet is represented using the Volume of Fluid (VoF) method proposed by Hirt et al. [18]. This chapter encompasses the governing equations and the applied overset method.

2.7.1. Governing equations

The continuity equation

$$\vec{\nabla} \cdot \vec{u} = 0\,, \tag{2}$$

with the nabla operator $\vec{\nabla}$ and the fluid's relative velocity vector

$$\vec{u} = \vec{u}_0 - \vec{u}_m\,, \tag{3}$$

where the difference between the absolute velocity $\vec{u}_0$ and the overset mesh velocity $\vec{u}_m$ is considered. Moreover, the momentum equation is expressed by

$$\frac{\partial}{\partial t}\left(\rho\,\vec{u}\right) + \vec{\nabla} \cdot \left(\rho\,\vec{u} \otimes \vec{u}\right) = -\vec{\nabla} p_d + \vec{\nabla} \cdot \boldsymbol{\tau} - \vec{g} \cdot \vec{x}\,\vec{\nabla}\rho + \vec{f}_\sigma\,, \tag{4}$$

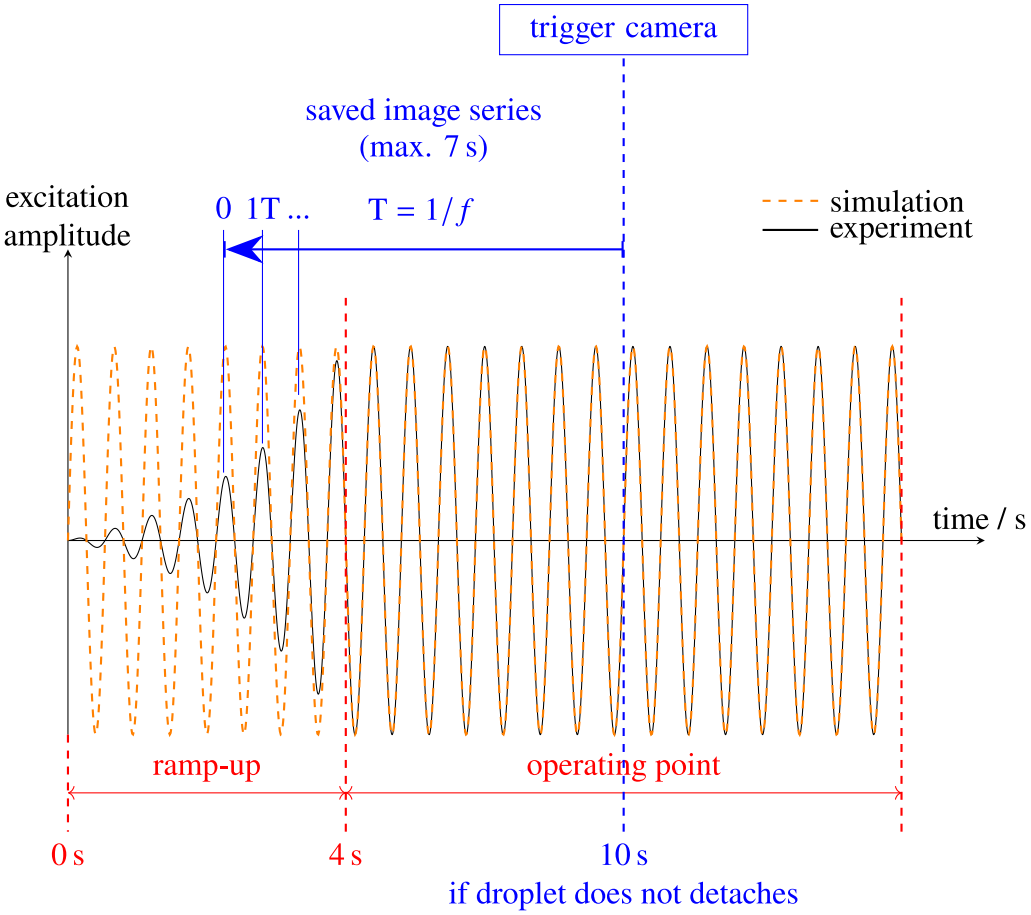

Fig. 4. Schematic sketch of relationship between time of excitation and saved timestamp of image series.

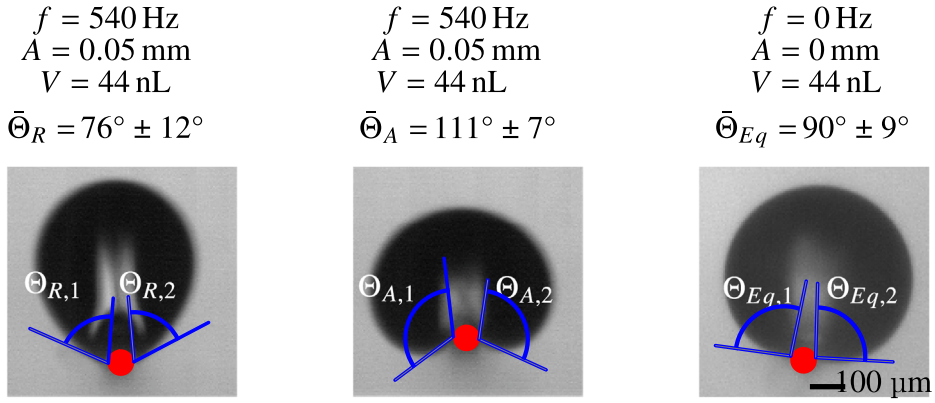

Fig. 5. Experimental measured receding (left), advancing (middle) and static (right) contact angle of an oil droplet on an oleophobic fiber (red).

including the distance vector from a reference position $\vec{x}$, the gravitational acceleration $\vec{g}$, the density of the mixture ρ, and the shear-rate tensor

$$\boldsymbol{\tau} = \mu \left[\vec{\nabla}\vec{u} + \left(\vec{\nabla}\vec{u} \right)^T \right], \tag{5}$$

the volumetric surface tension force $\vec{f}_\sigma$, the dynamic viscosity of the mixture μ, the velocity gradient $\vec{\nabla}\vec{u}$, and the reduced pressure p_d. The static pressure can be calculated by

$$p = p_d + \rho \vec{g}\, \vec{x}\,. \tag{6}$$

The solver *overInterDyMFoam* implements the VoF model for two fluids that can be assumed to be isothermal, immiscible and incompressible. The advection of the oil phase is determined by

$$\frac{\partial}{\partial t}(\alpha) + \vec{\nabla} \cdot (\alpha \vec{u}) + \vec{\nabla} \cdot \left[\vec{u}_r\, \alpha\, \alpha_p \right] = 0\,, \tag{7}$$

with the volume fraction of oil α, the volume fraction of air $\alpha_p = 1 - \alpha$ and a relative velocity vector between the two phases active in the interface region of the fluid u_r (for more information about the implementation, the reader is referred to Rusche [19]). Consequently, the local viscosity and density are calculated using the volumetric

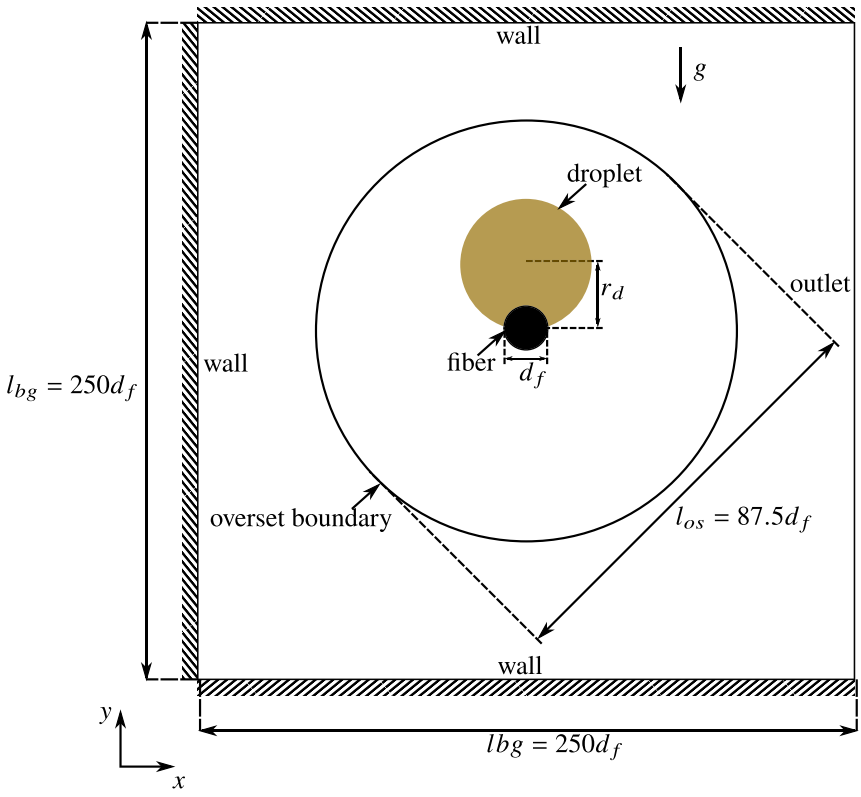

Fig. 6. Schematic drawing of the simulation setup under excitation at $f = 540\,\text{Hz}$ and $A = 0.05\,\text{mm}$.

average of the densities and viscosities of air (ρ_p, μ_p) and oil (ρ_s, μ_s) respectively:

$$\rho = \alpha\rho_s + \alpha_p\rho_p \tag{8}$$

$$\mu = \alpha\mu_s + \alpha_p\mu_p\,. \tag{9}$$

However, the surface tension force is implemented as a Continuum Surface Force (CSF) [20]

$$f_\sigma = \sigma\kappa\,\vec{\nabla}\alpha\,, \tag{10}$$

where σ is the surface tension coefficient, κ is the mean curvature of the free surface and $\vec{\nabla}\alpha$ is the secondary phase gradient. Notably, the divergence of the normalized gradient of the secondary phase gradient is used to calculate the curvature in Eq. (10)

$$\kappa = -\vec{\nabla}\cdot\left(\frac{\vec{\nabla}\alpha}{\left|\vec{\nabla}\alpha\right|}\right). \tag{11}$$

2.7.2. Model set up

The two-dimensional simulation setup is illustrated in Fig. 6, depicting the side length of the background mesh $l_{bg} = 20\,\text{mm}$, the amplitude of oscillation A, the fiber diameter d_f, the droplet radius r_d, and the gravitation g. The droplet starts on top of the fiber with the equilibrium contact angle Θ_{Eq} of 90°. Oil ($\rho_s = 875\,\text{kg m}^{-3}$, $\nu_s = 1.55\cdot10^{-4}\,\text{m}^2\,\text{s}^{-1}$, $\sigma = 0.0382\,\text{N m}^{-2}$) was used for the droplet, and air ($\rho_p = 1\,\text{kg m}^{-3}$, $\nu_p = 1.48\cdot10^{-5}\,\text{m}^2\,\text{s}^{-1}$) as the surrounding medium, both at sea level pressure (1 atm) and room temperature (20 °C). The surface tension coefficient σ was considered constant and determined experimentally. Additionally, the average advancing contact angle $\Theta_A = 111°$ and receding contact angle $\Theta_R = 76°$ were used for the simulation. To set the initial phase fraction $\alpha = 1$ for the oil in the two-dimensional simulations, the droplet volume V was used to calculate a sphere volume equivalent radius

$$r_d = \left(\frac{V}{\frac{4}{3}\pi}\right)^{\frac{1}{3}}, \tag{12}$$

Table 2
Boundary conditions for the overset simulation.

Boundary	Pressure p_d	Velocity u	Oil volume fraction α
outlet	$p_d = 0$	$\frac{\partial\vec{u}}{\partial\vec{n}} = 0$	$\frac{\partial\alpha}{\partial\vec{n}} = 0$
wall	$\frac{\partial p_d}{\partial\vec{n}} = 0$	$\vec{u} = \vec{0}$	$\frac{\partial\alpha}{\partial\vec{n}} = 0$
fiber	$\frac{\partial p_d}{\partial\vec{n}} = 0$	$\vec{u} = \vec{u}(t)$	$\frac{\partial\alpha}{\partial\vec{n}} = 0$

resulting in a small error (< 5% of the droplet area) when initiating the droplet because of the overlap with the fiber's area, which is expected to be insignificant.

The mesh motion capability of the solver was utilized, so that the fiber together with the overset mesh is moving in y-direction according to

$$y(t) = A\,sin\,(2\,\pi\,f\,t)\,, \tag{13}$$

with the amplitude A, the frequency f and the time t. Three of the outer boundaries of the background mesh are declared as walls with a no-slip boundary condition; the other side is declared as an outlet with a Dirichlet condition for reduced pressure and a Neumann boundary condition for velocity (see Table 2). The overset boundary is interpolated from the background grid using the inverse distance scheme; the fiber boundary of the overset mesh is a wall, moving with the velocity of the overset mesh (calculated utilizing Eq. (13) for mesh displacement).

For the spatial discretization, second-order linear schemes were applied to all gradients and divergence operations, except for the diffusive term of the momentum equation, which was discretized using a first-order upwind scheme. In terms of time discretization, a first-order accurate implicit Euler scheme was employed.

The simulations were conducted using a dynamic timestep, keeping the Courant number lower than 0.5. Furthermore, the time step was

Table 3
Number of cells in the different grid types for mesh convergence analysis.

Type	Overset	Background	Total
coarse	10,500	18,172	28,672
medium	30,000	27,819	57,918
fine	45,000	70,420	115,420

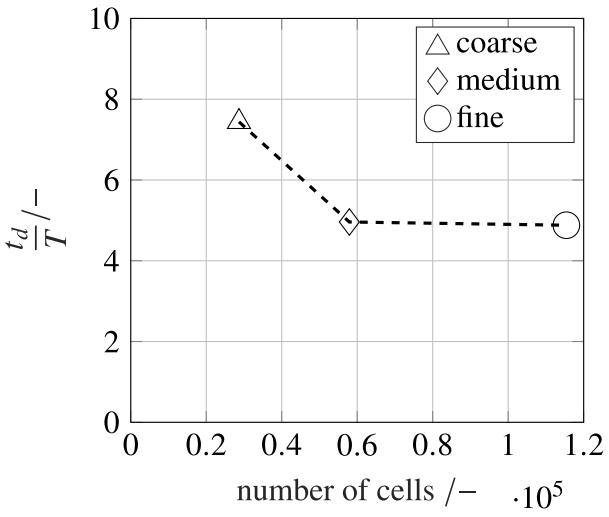

Fig. 7. Results of the mesh sensitivity analysis.

limited by the capillary time step [20]

$$\Delta t_\sigma = \sqrt{\frac{(\rho_p + \rho_s)\, V_{min}}{4\pi\sigma}} \tag{14}$$

with the volume of the smallest cell V_{min}.

2.8. Mesh sensitivity analysis

A mesh sensitivity analysis is conducted to determine the most suitable mesh for the simulations. Three different meshes, as listed in Table 3, were used. To ensure good overset interpolation quality, the mesh is refined to make sure that the ratio $\frac{V_{ac}}{V_{dc}}$ between the volumes of the acceptor cell V_{ac} and the donor cells V_{dc} does not exceed 5. Due to the unidirectional movement of the overset mesh region through the background mesh, the refinement zone has a rectangular shape. This configuration ensures uniform cell refinement along the fiber's trajectory. In total, the mesh is refined 6 times, once including the area covered by the overset boundary and five more times only including the area covered by the moving fiber. For the three different mesh setups, the background mesh maintained the same refinement zones, while the default number of cells in the background and overset region was increased.

To assess the performance of the different meshes, the simulation time needed until the droplet detaches from the fiber is computed. The results in Fig. 7 show that the droplet detaches in all three simulations. In the case of the coarse grid, the droplet requires a few additional periods of excitation until detaching from the fiber, where this time in the medium and fine cases is converging. The medium grid is computationally more efficient than the fine grid because it contains fewer cells and its greater grid spacing results in an increased time step, thus it is chosen for further simulations in this study.

Fig. 8 illustrates the overset mesh in blue and the background in black. Additionally, details of the inner and outer interpolation zones are shown on the sides.

3. Results

This section presents the various types of droplet motion observed on the oleophobic fiber, based on image sequences from individually selected experiments and simulations. For enhanced visibility, the fiber's position is highlighted by a red cross. It was decided to show the raw images for the experiments in order to avoid potential distortions caused by setting a threshold. On the other hand, a white ($\alpha = 0$) to black ($\alpha = 1$) mapping was used for the oil volume fraction (α) field in the simulations to create the images presented.

With a droplet of volume $V = 44\,\text{nL}$, an excitation frequency of $f = 100\,\text{Hz}$ and an amplitude of $A = 0.05\,\text{mm}$, the droplet remains nearly static on the fiber (see Fig. 9). In this state, the droplet assumes a clamshell-shaped configuration while resting on the fiber, exhibiting no noticeable deformation or change in the relative position of the droplet to the fiber. As the droplet volume increases, even slight deviations from an ideal, symmetric placement on the fiber give rise to a progressively larger torque about the droplet's center of mass when excitation begins. In the near-static example shown here in Fig. 9, however, the contact line remains pinned, and the droplet undergoes virtually no deformation despite its eccentric positioning. Similarly, the advancing and receding contact angles remain unchanged.

For a droplet with a volume of $V = 44\,\text{nL}$ subjected to an excitation with a frequency of $f = 540\,\text{Hz}$ and an amplitude of $A = 0.05\,\text{mm}$, the droplet undergoes a deformation in which it periodically elongates and contracts (pumping). The droplet elongates along the vector formed by the droplet's and the fiber's center of mass. During contraction, the fiber moves towards the area of the center of mass, resulting in the formation of a visible notch (see Fig. 10). As a result, the advancing and receding contact angles change by the equal amount.

The droplet also tilts around the fiber (swinging), as observed in Fig. 11. In this case, the droplet does not fully enclose the fiber, retaining its clamshell-like structure in a more distant sense.

Swinging and pumping can also occur simultaneously, particularly when the droplet is asymmetrically positioned on the fiber surface and the excitation of the fiber is applied eccentrically.

In general, there are two distinct mechanisms by which a droplet can fully surround a cylindrical fiber. First, the droplet's three-phase contact lines move circumferentially toward each another until they meet and coalesce, thereby enclosing the liquid around the fiber. Second, the droplet deforms globally to wrap around the fiber before the three-phase contact lines move circumferentially and touch one another. Notably, the initial droplet position does not influence whether the transition occurs.

Fig. 12 illustrates how the pumping motion causes the droplet to deform, leading to complete fiber enclosure. In the final image of the series, the fiber position, marked in red, is located within the droplet, indicating the formation of a barrel-shaped droplet. Fig. 13 shows the two droplet contact angles in the simulation over a dimensionless time $\frac{t}{T}$ for the few periods leading up to the droplet transition (happening at $t/T = 0$. The contact angles are calculated using an $\alpha = 0.5$-iso contour and its angle to the fiber surface. Both contact angles exhibit a similar, symmetric evolution and oscillate with the same frequency as the fiber until they meet, at which point the droplet transitions to a barrel-shape.

Furthermore, Fig. 14 highlights a 44 nL droplet that transitions from a clam-shell shape to a barrel-shape. In this case, the droplet transitions while swinging around the fiber. Fig. 15 shows the contact angles of the droplet in the simulation over a dimensionless time leading up to the transition (happening at $t/T = 0$). Characteristic for a swinging droplet, there is one advancing and one receding contact angle, which switch when the direction the swing changes. It is also evident that the droplets contact angle oscillation has a frequency of about half the excitation frequency, so its oscillations takes about $2T$. The transition of the droplet happens at a point, where the advancing contact and the receding contact angle are at a maximum and minimum, respectively.

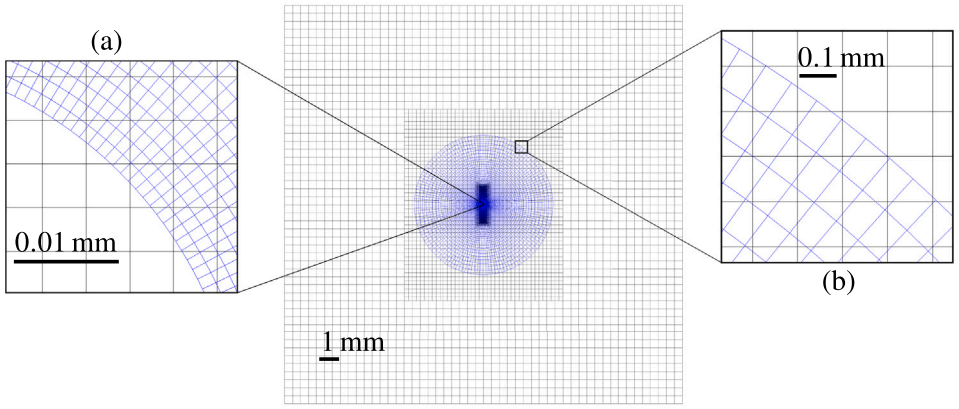

Fig. 8. Mesh with details of the inner interpolation zone (a) and outer interpolation zone (b).

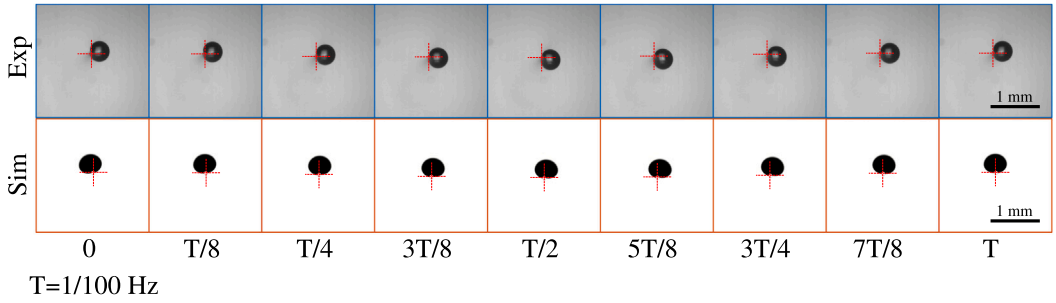

Fig. 9. Static droplet on the oleophobic fiber with a volume of $V = 44\,\text{nL}$ under excitation at $f = 100\,\text{Hz}$ and $A = 0.05\,\text{mm}$.

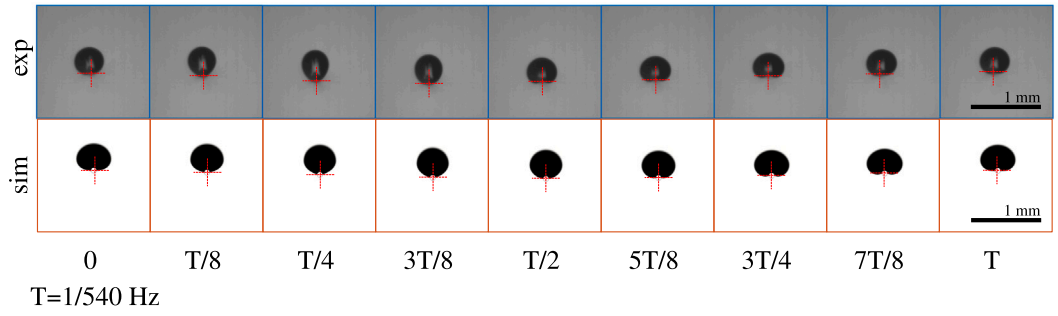

Fig. 10. Pumping of a droplet on the oleophobic fiber for a droplet with $V = 44\,\text{nL}$ under excitation at $f = 540\,\text{Hz}$ and $A = 0.05\,\text{mm}$.

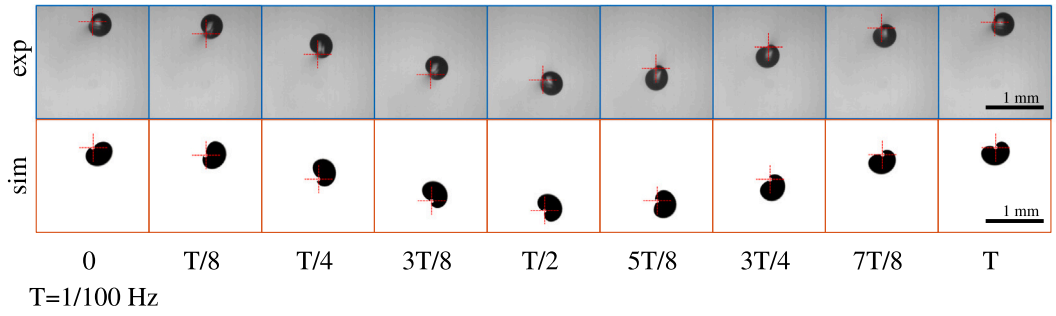

Fig. 11. Swinging of a droplet around the oleophobic fiber for a droplet with $V = 44\,\text{nL}$ under excitation at $f = 100\,\text{Hz}$ and $A = 0.5\,\text{mm}$.

Fig. 16 highlights additional cases in which the droplet enclosed the fiber fully due to the mechanical excitation. As mentioned before, his occurs either through the pumping motion or via the swinging motion, in which the advancing front of the droplet swings around the fiber, catching up to the receding front. The data suggest that a clamp-shell shaped droplet transitions into a barrel-shaped droplet for the Reynolds

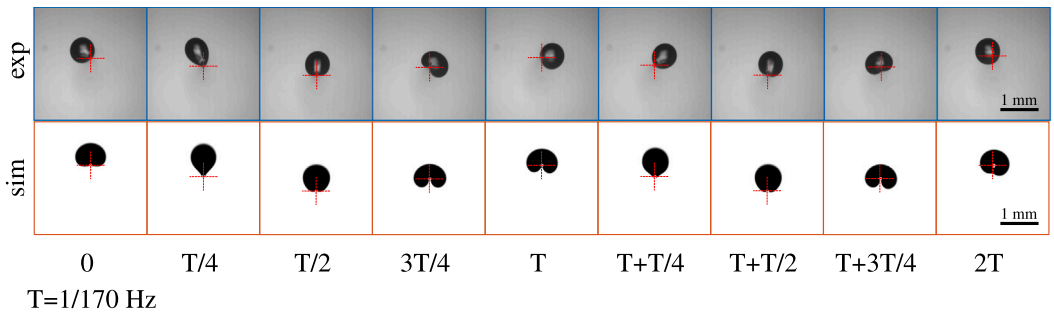

Fig. 12. Transition from a barrel-shaped to a clamshell-shaped droplet for a droplet with $V = 176\,\text{nL}$ on the oleophobic fiber under excitation at $f = 170\,\text{Hz}$ and $A_{exp} = 0.23\,\text{mm}$ and $A_{sim} = 0.3\,\text{mm}$.

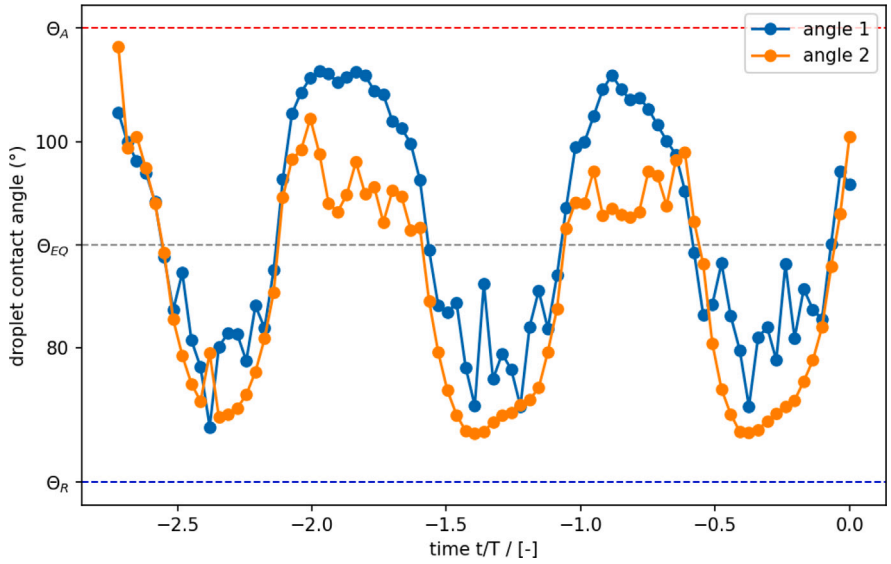

Fig. 13. Contact angle evolution of a 176 nL droplet on an excited fiber ($f = 170\,\text{Hz}$ and $A = 0.5\,\text{mm}$) concluding with the period shown in Fig. 12.

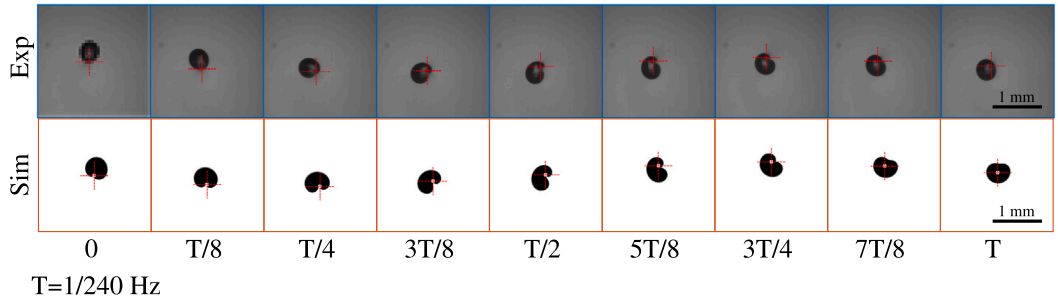

Fig. 14. Transition from a barrel-shaped to a clamshell-shaped droplet for a droplet with $V = 44\,\text{nL}$ on the oleophobic fiber under excitation at $f = 240\,\text{Hz}$ and $A = 0.25\,\text{mm}$.

number

$$Re = \frac{2\,\pi\,f\,A\,r_d}{\nu_s} \tag{15}$$

being higher than 0.4. Furthermore, a higher ratio $\frac{r_d}{r_f}$ seems to enable the droplet transition for lower Reynolds numbers.

Due to the enclosure of the fiber, the simulation results show that air becomes trapped inside the droplet, which could be a result of the dimension reduction. Additionally, there was no entrapment detected in the experiments using the available imaging techniques.

In further repeated experiments, it was investigated whether the droplet transitions back from a barrel-shaped droplet to a clamshell-shaped droplet when the excitation is stopped. After the transition, the droplet was observed on the stationary fiber for at least 24 h. However, this reversal was not observed. For all investigated droplet volumes, the droplet remained in the barrel shape.

Once the droplet has completely enclosed the fiber, movement patterns similar to those described in [17] for an oleophilic fiber are observed. Depending on the excitation strength and the droplet size, the droplet can exhibit vertical oscillation, rotation, and collapse (multiple times) from the rotating motion on the fiber. The experimental results show no influence on the occurrence of these mechanisms by the initial droplet position on the fiber.

Vertical oscillation is depicted in Fig. 17. The droplet maintains an almost symmetrical shape along the vertical axis. As a result of the excitation, the fully enclosed fiber moves periodically up and down inside the droplet.

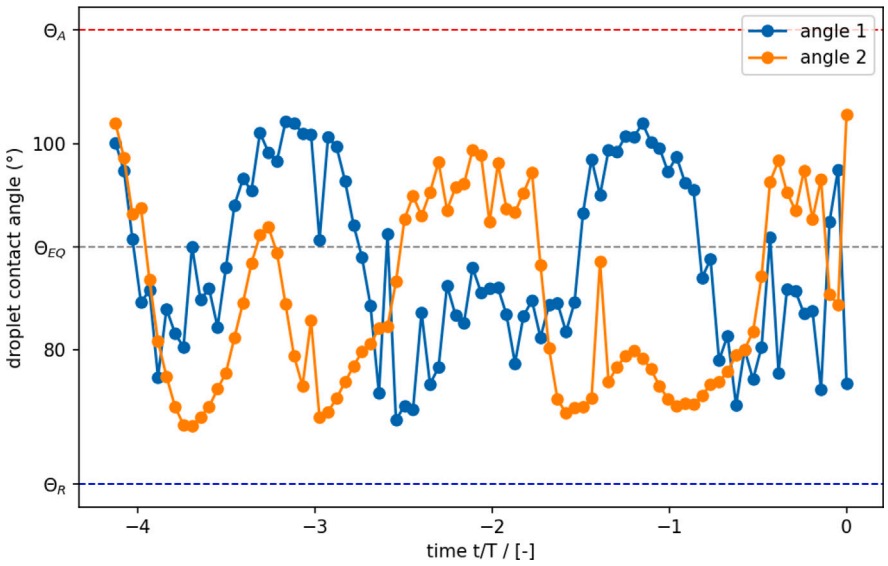

Fig. 15. Contact angle evolution of a 44 nL droplet on an excited fiber ($f = 240$ Hz and $A = 0.25$ mm) concluding with the period shown in Fig. 14.

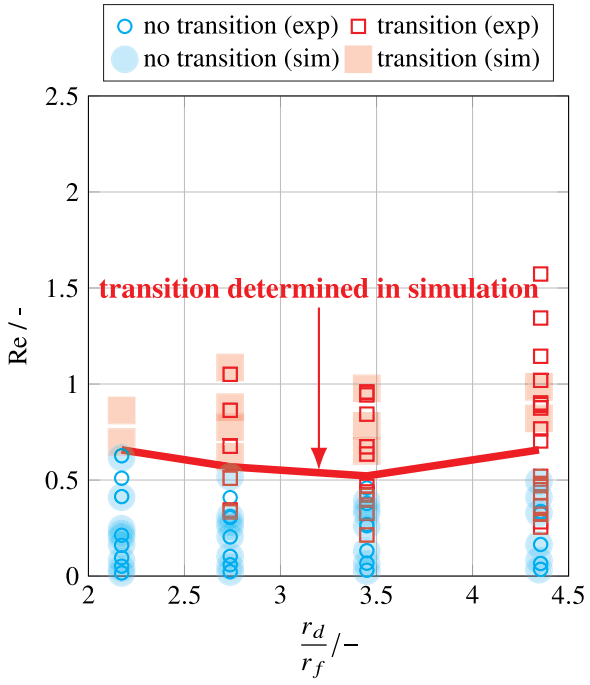

Fig. 16. Transition map clamp-shell shaped to barrel-shaped oil droplet on an oleophobic fiber.

If the droplet's contour is asymmetrical relative to the excitation axis, the droplet accelerates eccentrically and starts moving around the fiber. For higher accelerations, this results in the droplet performing full rotations around the fiber, as shown in Fig. 18.

Finally, the droplet may detach from the fiber due to the rotational motion. If detachment does not occur, the rotation can be intermittently disrupted, leading to the droplet's collapse, as shown in Fig. 19.

As demonstrated by the image sequences, a droplet can exhibit various motion patterns on the fiber depending on the excitation parameters. The reported motion patterns observed by [17] for an oleophilic fiber are summarized in the upper part of Fig. 20, where the relative position of the area center of mass of the fiber and droplet in the y direction $\Delta C_y/d_f$ is plotted against the x direction $\Delta C_x/d_f$. In comparison, all motion patterns occurring in this study for a droplet on an oleophobic fiber are shown in the lower part of Fig. 20 in the same manner. Starting from a static position, the droplet transitions through the movement patterns reported in Fig. 20 from left to right as it is placed on a resting fiber and subsequently excited sufficiently. Considering the stability of these motion patterns, they can be classified as either stable or unstable. A motion pattern is considered stable if the droplet remains in this state under constant excitation until the excitation parameters change. If the motion pattern changes despite constant excitation or if the droplet detaches from the fiber, the motion state is considered unstable. According to the definition of stability, the transition is not a stable motion pattern.

Additionally, droplet detachment from the fiber was observed following a rotational motion around the fiber; therefore, this motion pattern is also not stable. In some cases, instead of detaching, the droplet collapsed on the fiber after undergoing rotational motion. For a droplet collapsing (multiple times) on the fiber, two observations can be made: first, the droplet eventually detaches from the rotational motion; second, within the observed time frame, the droplet does not detach. However, it is assumed that with a longer excitation duration, the droplet will always detach after collapsing multiple times. Thus, only the motion patterns static, pumping & swinging, and vertical oscillation are considered to be stable.

Fig. 21 compares droplet detachment and adherence behavior for both oleophobic and oleophilic fibers by plotting the Reynolds number Re (Eq. (15)) against the droplet-to-fiber radius ratio $\frac{r_d}{r_f}$. For higher Re, when the ratio of the impulse forces and viscus forces rises, the detachment of the droplet is enabled. Furthermore the results of both, simulations and experiments, suggest the ratio of $\frac{r_d}{r_f}$ has to be higher than 2.5 for droplet detachment to occur. These findings are limited to the analyzed Re regime and it is possible for a droplet with $\frac{r_d}{r_f} < 2.5$ to detach for higher Re.

4. Conclusion

This study examined the influence of vibration on the wetting behavior of single oil droplets on an oleophobic fiber, revealing additional motion patterns compared to oleophilic fibers. The results demonstrate that droplets undergo various dynamic behaviors, including pumping, swinging, vertical oscillation, rotation, and (reoccurring) collapse, depending on excitation parameters.

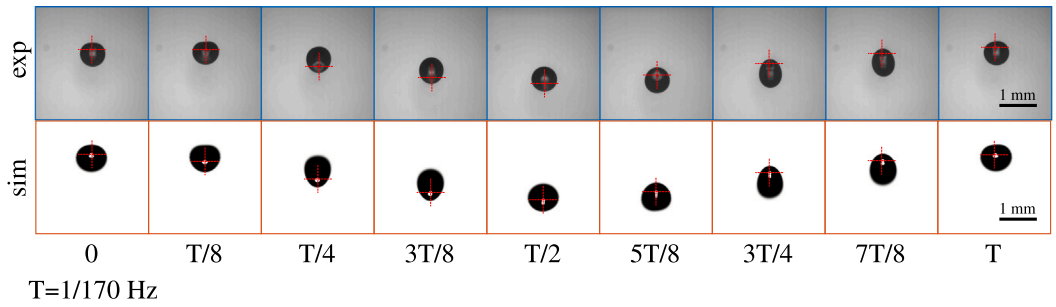

Fig. 17. Vertical oscillation of a droplet around the fiber for a droplet with $V = 176\,\text{nL}$ under excitation at $f = 170\,\text{Hz}$ and $A = 0.5\,\text{mm}$.

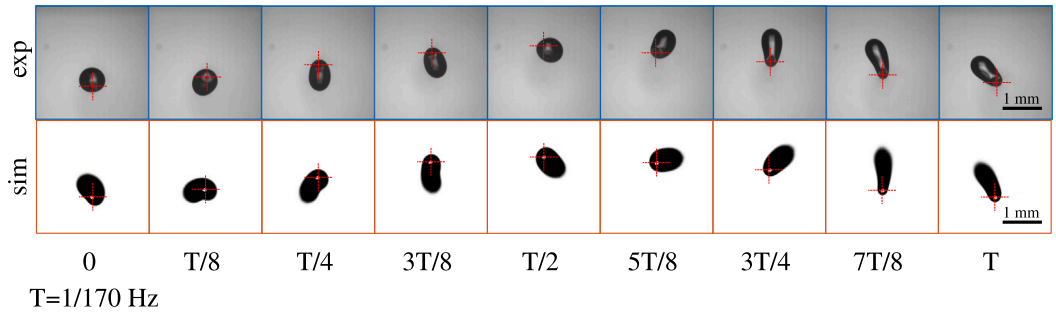

Fig. 18. Rotational movement of a droplet around the fiber for a droplet with $V = 176\,\text{nL}$ under excitation at $f = 170\,\text{Hz}$ and $A = 0.5\,\text{mm}$.

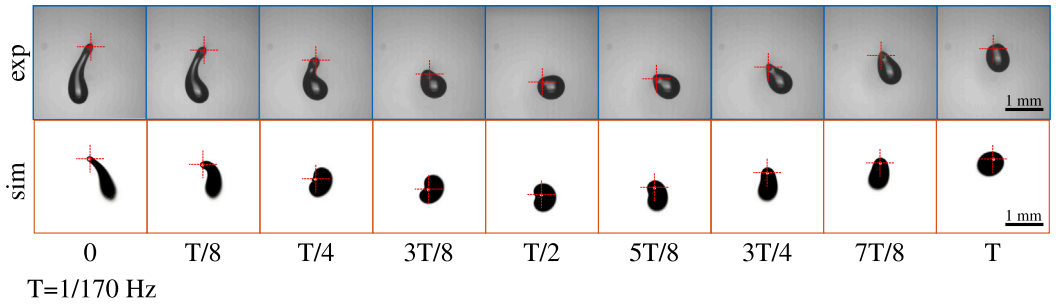

Fig. 19. Collapsing of a droplet on the oleophobic fiber for a droplet with $V = 176\,\text{nL}$ under excitation at $f = 170\,\text{Hz}$ and $A = 0.5\,\text{mm}$.

A key finding is that fiber excitation can induce a lasting transition from a barrel-shaped droplet to a clamshell-shaped droplet. Furthermore, the study revealed that after the transition, prior to detachment, a droplet exhibits identical motion patterns and wetting behavior on both oleophilic and oleophobic fibers. This suggests that, for the material system investigated here, droplet detachment occurs under similar excitation conditions, regardless of fiber wettability.

5. Outlook

Future research should explore the influence of additional external factors on droplet–fiber interactions under vibration. One key aspect is the effect of an external gas flow, which could impact droplet motion, detachment behavior, and wetting dynamics. Investigating this influence experimentally and numerically would provide deeper insights into practical applications, such as filtration systems.

Additionally, extending the study to a multi-fiber structure or a real filter environment could help assess how the observed motion patterns evolve in more complex systems. Understanding droplet behavior in such environments would be particularly relevant for optimizing coalescence and drainage processes in industrial filtration applications.

Future investigations could employ three-dimensional simulations to understand the transition behavior and its prerequisites further.

CRediT authorship contribution statement

Florian Freese: Writing – review & editing, Writing – original draft, Visualization, Validation, Supervision, Software, Resources, Project administration, Methodology, Investigation, Funding acquisition, Formal analysis, Data curation, Conceptualization. **Alexander Schwarzwälder:** Writing – review & editing, Writing – original draft, Visualization, Validation, Supervision, Software, Resources, Project administration, Methodology, Investigation, Funding acquisition, Formal analysis, Data curation, Conceptualization. **Uwe Janoske:** Writing – review & editing, Supervision, Project administration, Funding acquisition. **Achim Dittler:** Writing – review & editing, Supervision, Project administration, Funding acquisition.

Declaration of competing interest

The authors declare that they have no known competing financial interests or personal relationships that could have appeared to influence the work reported in this paper.

Acknowledgment

This work was financially supported by the Deutsche Forschungsgemeinschaft (DFG), Germany as part of the project 499469405.

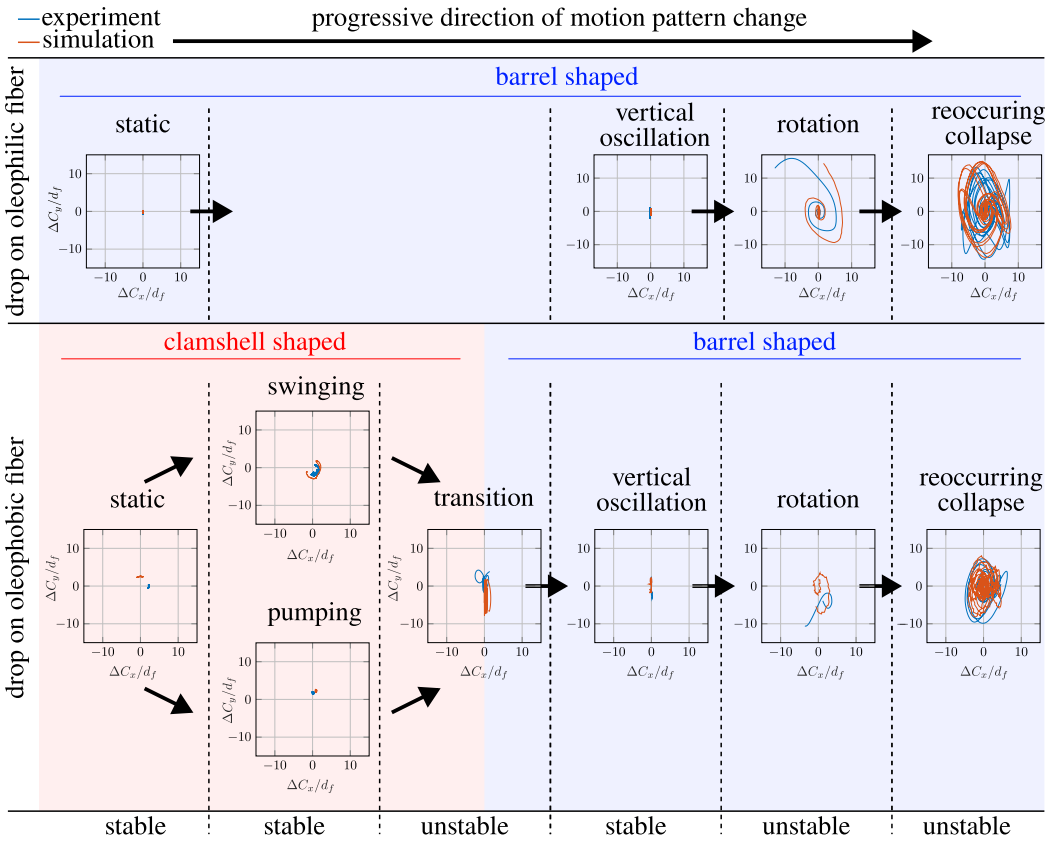

Fig. 20. Observed motion patterns of an oil droplet on an excited oleophilic fiber (top) and an oleophobic fiber (bottom).

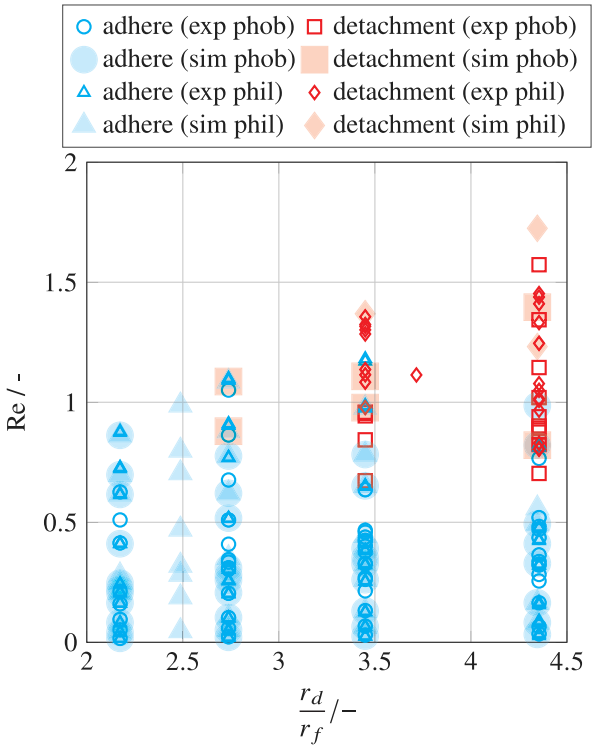

Fig. 21. Detaching vs adhering droplets plotted as Re over $\frac{r_d}{r_f}$ on an oleophobic and oleophilic fiber.

Appendix. Determination of the natural frequency

Given Values

- Length of the fiber: $L = 0.04\,\mathrm{m}$
- Diameter of the fiber: $d = 8 \cdot 10^{-5}\,\mathrm{m}$
- Material of the fiber: 1.4301 (Stainless Steel)
  - Density: $\rho = 7900\,\mathrm{kg\,m^{-3}}$
- Mass of weight for inducing tensile force: $m = 0.25\,\mathrm{kg}$

The natural frequency f_n [21,22] of a string with the mode number n can be calculated as

$$f_n = \frac{n}{2L} \cdot \sqrt{\frac{F}{\rho \cdot A}},$$

where F is the tensile force, L the length, A the cross section area, and ρ the density of the fiber.

$f_1 = 3.11 \cdot 10^3\,\mathrm{Hz}$

Data availability

Data will be made available on request.

References

[1] C. Straube, J. Meyer, A. Dittler, Identification of deposited oil structures on thin porous oil mist filter media applying μ-ct imaging technique, Separations 8 (10) (2021) http://dx.doi.org/10.3390/separations8100193.

[2] R. Akbari, C. Antonini, Contact angle measurements: From existing methods to an open-source tool, Adv. Colloid Interface Sci. 294 (2021) 102470, http://dx.doi.org/10.1016/j.cis.2021.102470.

[3] N.M. Farhan, H. Aziz, H.V. Tafreshi, Simple method for measuring intrinsic contact angle of a fiber with liquids, Exp. Fluids 60 (5) (2019) http://dx.doi.org/10.1007/s00348-019-2733-2.
[4] J.W. Drelich, L. Boinovich, E. Chibowski, C. Della Volpe, L. Hołysz, A. Marmur, S. Siboni, Contact angles: history of over 200 years of open questions, Surf. Innov. 8 (1–2) (2020) 3–27, http://dx.doi.org/10.1680/jsuin.19.00007.
[5] G. McHale, S. Rowan, M. Newton, N. Käb, Estimation of contact angles on fibers, J. Adhes. Sci. Technol. 13 (1999) 1457–1469, http://dx.doi.org/10.1163/156856199X00587.
[6] A. Bick, F. Boulogne, A. Sauret, H.A. Stone, Tunable transport of drops on a vibrating inclined fiber, Appl. Phys. Lett. 107 (18) (2015) http://dx.doi.org/10.1063/1.4935251.
[7] P. Zhu, W. Wang, X. Chen, F. Lin, X. Wei, C. Ji, J. Zou, Experimental study of drop impact on a thin fiber, Phys. Fluids 31 (10) (2019) http://dx.doi.org/10.1063/1.5116845.
[8] L. Feng, Y. Jiang, C. Machado, W. Choi, N.A. Patankar, K.-C. Park, Directional self-propelled transport of coalesced droplets on a superhydrophilic cylindrical wire, Tech. rep., Northwestern University, 2022.
[9] M.M. Amrei, D.G. Venkateshan, N. D'Souza, J. Atulasimha, H.V. Tafreshi, Novel Approach to Measuring the Droplet Detachment Force from Fibers, Langmuir 32 (50) (2016) 13333–13339, http://dx.doi.org/10.1021/acs.langmuir.6b03198.
[10] M.M. Amrei, M. Davoudi, G.G. Chase, H.V. Tafreshi, Effects of roughness on droplet apparent contact angles on a fiber, Sep. Purif. Technol. 180 (2017) 107–113, http://dx.doi.org/10.1016/j.seppur.2017.02.049.
[11] H.B. Eral, J. De Ruiter, R. De Ruiter, J.M. Oh, C. Semprebon, M. Brinkmann, F. Mugele, Drops on functional fibers: From barrels to clamshells and back, Soft Matter 7 (11) (2011) 5138–5143, http://dx.doi.org/10.1039/c0sm01403f.
[12] Y. Sun, K.G. Kornev, Does the contact angle hysteresis control the droplet shapes on cylindrical fibers? Colloids Surfaces A: Physicochem. Eng. Asp. 668 (2023) http://dx.doi.org/10.1016/j.colsurfa.2023.131435.
[13] N.M. Farhan, H.V. Tafreshi, Using Magnetic Field to Measure Detachment Force between a Nonmagnetic Droplet and Fibers, Langmuir (2019) http://dx.doi.org/10.1021/acs.langmuir.9b01313.
[14] S. Poulain, A. Carlson, Sliding, vibrating and swinging droplets on an oscillating fibre, J. Fluid Mech. 967 (2023) http://dx.doi.org/10.48550/arXiv.2210.06314.
[15] J.K. Park, K.H. Kang, Numerical analysis of moving contact line with contact angle hysteresis using feedback deceleration technique, Phys. Fluids 24 (4) (2012) http://dx.doi.org/10.1063/1.4707703.
[16] V. Krämer, B. Barwari, S. Burgmann, M. Rohde, S. Rentschler, C. Holzknecht, C. Gmelin, U. Janoske, Numerical analysis of an adhering droplet applying an adapted feedback deceleration technique, Int. J. Multiph. Flow 145 (2021) http://dx.doi.org/10.1016/j.ijmultiphaseflow.2021.103808.
[17] A. Schwarzwaelder, F. Freese, J. Meyer, K. Loganathan, H. Tietze, A. Dittler, U. Janoske, Experimental and numerical investigation of droplet–fiber interaction on mechanically excited fiber, Phys. Fluids 36 (3) (2024) http://dx.doi.org/10.1063/5.0188784.
[18] C. Hirt, B. Nichols, Volume of fluid (VOF) method for the dynamics of free boundaries, J. Comput. Phys. 39 (1) (1981) 201–225, http://dx.doi.org/10.1016/0021-9991(81)90145-5.
[19] H. Rusche, Computational Fluid Dynamics of Dispersed Two-Phase Flows at High Phase Fractions (Ph.D. thesis), Imperial College London, London, 2003.
[20] J.U. Brackbill, D.B. Kothe, C. Zemach, A Continuum Method for Modeling Surface Tension*, Tech. rep., NASA Lewis Research Center Cleveland, 1992.
[21] K. Königsberger, Analysis 1, Springer Berlin Heidelberg, Berlin, Heidelberg, 1990, http://dx.doi.org/10.1007/978-3-642-97217-1.
[22] O. Forster, Analysis 2, Springer Fachmedien Wiesbaden, Wiesbaden, 2017, http://dx.doi.org/10.1007/978-3-658-19411-6.